



Quantitative Nondestructive Evaluation of Cold Spray Manufactured Aluminum Alloy 6061 and Copper Samples

Kishore Kumar Indu Kumar¹ · Mann Baijukumar Patel¹ · Samuel Boese² · Andrew Gouldstone¹ · Victor K. Champagne Jr.³ · Ozan Ç. Özdemir¹ 

Submitted: 15 August 2023 / in revised form: 20 January 2024 / Accepted: 22 January 2024 / Published online: 28 February 2024
© The Author(s) 2024

Abstract Cold spray (CS) is a solid-state process for depositing thick layers of material via the successive high-velocity impact of powder particles onto a solid surface, which leads to high rates of deformation, interparticle bonding, and coating build-up. Although CS is finding commercial utilization in non-load-bearing repair and coating applications, clear nondestructive characterization procedures are necessary to realize its potential in load-bearing structural applications. In this study, the viability of electrical conductivity and through thickness ultrasound wave velocity measurement methods was studied to serve as a means for nondestructive quantitative measurement for quality control in CS and potentially other additive manufacturing (AM) methods. Eddy current, ultrasound, porosity, hardness, and uniaxial tensile strength tests were

conducted on CS deposited layers of aluminum alloy 6061 and copper on aluminum alloy 6061 and commercially pure copper substrates, respectively. CS gas dynamic parameters were intentionally and systematically varied to result in corresponding discrete differences in mechanical properties of deposits. Ultrasound measurements of longitudinal wave velocity and eddy current electrical conductivity measurements showed good correlation with process conditions, microstructural characterization results, and destructive mechanical tests (hardness, tensile). The results of this work show that ultrasound wave velocity and electrical conductivity correlate well with increased particle impact velocity in CS deposited aluminum and copper blocks, which evidently show an incremental decrease in porosity, increase in hardness, and increase in tensile strength. The outlined ultrasound and eddy current non-destructive testing methods present effective means for quantitative assessment of cold spray deposited structures while intact with the substrate.

Keywords cold spray · eddy current · electrical conductivity · nondestructive testing · quantitative · ultrasound

This article is an invited paper selected from presentations at the 2023 International Thermal Spray Conference, held May 22-25, 2023, in Québec City, Canada, and has been expanded from the original presentation. The issue was organized by Giovanni Bolelli, University of Modena and Reggio Emilia (Lead Editor); Emine Bakan, Forschungszentrum Jülich GmbH; Partha Pratim Bandyopadhyay, Indian Institute of Technology, Karaghpur; Šárka Houdková, University of West Bohemia; Yuji Ichikawa, Tohoku University; Heli Koivuluoto, Tampere University; Yuk-Chiu Lau, General Electric Power (Retired); Hua Li, Ningbo Institute of Materials Technology and Engineering, CAS; Dheepa Srinivasan, Pratt & Whitney; and Filofteia-Laura Toma, Fraunhofer Institute for Material and Beam Technology.

✉ Ozan Ç. Özdemir
o.ozdemir@northeastern.edu

¹ Department of Mechanical and Industrial Engineering, Northeastern University, Boston, MA, USA

² Kostas Research Institute, Burlington, MA, USA

³ U.S. Army Research Laboratory, Aberdeen, MD, USA

Introduction

CS is a line-of-sight solid-state material deposition process that enables the deposition of primarily metals and metal matrix composites (Ref 1-3), but also polymers (Ref 4) and ceramics (Ref 5), by means of kinetic impact energy dissipation. In CS, microscale particles ($\sim 5\text{-}100\ \mu\text{m}$) are accelerated to velocities in the range of 300-1500 m/s by introducing them into a compressed gas stream that is expanded to sonic/supersonic velocities through converging

or converging-diverging De Laval spray nozzles (Ref 6-8). Upon impact on a surface or on previously deposited particles, high levels of contact pressure, shear, and thermal energy are created at the contact interface where extreme plastic deformation and material flow is experienced (Ref 9-11). Metal particles that exceed a critical velocity bond metallurgically and mechanically. While chemical and mechanical bonding can be seen in the deposition of polymers, ceramics that can be successfully deposited show signs of bonding solely due to mechanical interlocking. By manipulating the spray nozzle by hand or robot, and therefore, controlling the deposition location, CS can be used for coatings, part restoration, or near-net shaped part manufacturing (Ref 12-15). Although CS is increasingly proving applicable in the deposition of coatings and non-load-bearing repair applications (Ref 3, 12, 16-18) and in fast freeform manufacturing (Ref 19), expanding the technology to load-bearing repairs and manufacturing freeform structural components (3D printing) requires widely acceptable procedures for quality control.

Lack of generalized standardized procedures for ensuring process repeatability and reliability and product quality control are the most significant limiting factors to apply CS and other AM processes to a broad spectrum of load-bearing and machine critical components (Ref 20). Efforts in controlling the powder feedstock by far hold the biggest weight when it comes to standardizing CS processes because powder characteristics directly influence process parameter requirements. In CS, particle size distribution, shape distribution, and microstructural characteristics influence particle velocity and material deformation behavior, and therefore, influence the deposition density, adhesive and cohesive strength, and elastic behavior (Ref 21). As-deposited material properties also carry much of the feedstock properties owing to CS's solid-state nature. In AM processes, such as powder bed fusion (PBF), powder characteristics can influence energy absorption, sputtering, and surface quality (Ref 22). In the characteristics of powders of same materials, differences can originate from the manufacturer, powder batch, powder treatment, and powder classification. Therefore, some of the first standards that have been established for CS and AM processes are procedures for qualifying powders. Important examples include the MIL-DTL-32495 "Aluminum Powders for Cold Spray Deposition," and the ASTM-F3049-14 "Standard Guide for Characterizing Properties of Metal Powders Used for Additive Manufacturing Processes," which were later revised as MIL-DTL-32495A and ASTM-F3049-14R21, respectively. Furthermore, while the ASTM F42 and ISO TC261 technical committees have published standards on the design and qualification procedures for AM processes, the committees' recommendations are for rigorous functionality,

surface, thermomechanical, and microstructural analysis of AM manufactured parts via destructive tests with reference to x-ray Computed Tomography scanning to nondestructively check for internal flaws as given in ISO/ASTM 52901:2016(E) "Standard Guide for Additive Manufacturing—General Principles—Requirements for Purchased AM Parts." However, the large number of variables associated with CS and other AM methods and the increasingly large number of equipment manufacturers joining the market raise concern that unconventional manufacturing methods with added variables introduced by different machines can produce unexpected anomalies. Furthermore, nanoscale defects that may be present at particle-particle interfaces in CS and solid-state sintering processes (e.g., Selective Laser Sintering) cannot be captured simply using x-ray CT. Therefore, to establish CS and other AM methods as reliable manufacturing methods, nondestructive quality control measures need to be developed to ensure all CS and AM produced critical components that carry load undergo a thorough evaluation that can provide quantitative assessment of AM products.

Classic nondestructive methods, such as die penetrant, magnetic particle, eddy current, ultrasound testing, and computed tomography, can be used to identify major surface and subsurface defects qualitatively after post-spray machining in CS (Ref 13). Furthermore, laser ultrasonics and other optical sensors can provide *in-situ* or *ex-situ* dimensional information (Ref 23). However, when used for anomaly detection, these methods do not provide a quantitative means for quality control. In the quantitative non-destructive measurement of CS products, electrical conductivity measurements have been shown to prove a reliable method for indicating changes to the deposition structure as a result of process variables and/or post-process heat treatment procedures (Ref 24-27). Electrical conductivity can be a good indicator for detecting the level of underlying porosity (Ref 25, 28-30), presence of oxides (Ref 31), particle-particle interfacial bonding (Ref 27, 32, 33), and tensile strength (Ref 27). However, non-destructive electrical conductivity measurements are commonly performed using eddy current methods, which magnetically induce electrical currents near the surface and limit the material probing distance generally to less than 1 mm depending on eddy current frequency and power. Glass, et al. (Ref 24) and Maev, et al. (Ref 34) have noted that acoustic methods (e.g., ultrasound), on the other hand, can provide a quantitative means for nondestructively evaluating changes in the deposit microstructure in CS. Glass, et al. (Ref 24) noted that ultrasound wave velocity as well as signal attenuation can be indicative of differences in deposits. Clavette et.al. (Ref 35), reported that acoustic emission (AE) was used successfully to monitor the cold spray powder deposition process as a means to consider

defect detection as early as possible, in a complex, noisy environment. Similar to CS, Honarvar and Varvani-Farahani (Ref 36) report that, ultrasound wave velocity correlates well with porosity levels in powder bed fusion manufactured components. Although the use of eddy current and acoustic methods is reported to be valuable in quantitatively measuring deposition quality in CS and other AM processes, more attention is needed in correlating the sensitivity of the nondestructive methods to the process variabilities and the deposition properties.

Therefore, in this study, the sensitivity of electrical conductivity and ultrasound wave velocity is examined for aluminum alloy 6061 (Al6061) and commercially pure copper (Cu) cold spray deposits that were produced by varying particle impact velocity by means of manipulating process gas type, pressure, and temperature. Microstructural and mechanical analyses were performed to correlate porosity, material deformation, hardness, and tensile properties to ultrasound wave velocity and electrical conductivity.

Experimental Methods

Cold Spray Process and Velocity Measurements

Particle impact velocity, V_p is the most influential parameter in CS for material deformation and bond strength (Ref 37). This parameter is controlled indirectly by manipulating process gas pressure and temperature, which in turn influence particle drag and acceleration in spray nozzles. Here, a Gen III model high pressure CS system from VRC Metal Systems (Box Elder, SD) was used to deposit Al6061 and Cu samples by varying process conditions to change the particle impact velocity (V_p). A quasi-one-dimensional analytical process model (Ref 38) was used to guide and estimate V_p , which was used to adjust process parameters to induce different levels of material deformation and therefore deposition quality. V_p was compared with a semi-empirical critical velocity (V_{cr}) estimation (Ref 39), which defines the velocity required for bonding.

For this study, Al6061 powder was procured from Valimet (Stockton, CA, U.S.A.) and commercially pure Cu powder was procured from Praxair Surface Technologies (Indianapolis, IN, U.S.A.). The one-dimensional analytical model requires an understanding of the powder size and shape characteristics, which were measured using a Zeiss Axioscope 7 optical microscope (Oberkochen, Germany). The volumetric particle size distribution of powders is reported as D10, D50, and D90 values that represent the 10th, 50th, and 90th percentiles of particle size. Al6061 powder was measured to have D10, D50, and D90 values of 23.6 μm , 41.9 μm , and 57.1 μm , respectively, and an

average particle sphericity of 0.85. Here, sphericity is defined as the ratio of the area equivalent particle diameter to the major axis length of particles. The Praxair Cu powder on the other hand was measured to have D10, D50, and D90 values of 21.2 μm , 31.6 μm , and 40.2 μm , respectively, and an average sphericity value of 0.83. Nozzles recommended by the CS system manufacturer were used to handle Al6061 and Cu powders for nitrogen and helium. These are listed in Table 1 by providing the approximate nozzle expansion region dimensions significant for particle acceleration.

Al6061 was deposited at five different experimental conditions. CS process conditions were changed along with the substrate surface preparation method to introduce an additional degree of variability. Table 2 summarizes the selected gas type, gas pressure, gas temperature, surface preparation method and the estimated particle impact velocity. The N₂ spray condition for Al6061 was determined by maximizing the particle impact velocity for highest gas pressure and temperature condition limited by the maximum achievable pressure by the VRC Gen III system and the maximum operating temperature of the composite nozzle (NZZL0070). While 68 bar and 445 °C settings are not optimal, with a ratio of impact velocity to critical velocity (V_p/V_{cr}) of ~ 1.1 , these provide relatively dense material deposition and are used in common practice. To improve the adhesive strength of the Al6061 deposits, He was used with 35 bar and 445 °C at the nozzle, which provide a much-improved V_p/V_{cr} of ~ 1.4 . This is expected to also provide a major improvement in the mechanical properties of the deposit (Ref 40). While a higher than 1.4 V_p/V_{cr} is expected to provide better mechanical properties, the process settings were balanced to provide improved properties while conservatively using He due to its expense (Ref 41). Using the conditions given in Table 2, Al6061 powder was deposited on a 115 mm x 90 mm area using a serpentine raster pattern with a 1 mm line separation. After machining the top surfaces of the samples, deposition thicknesses of 3.24 mm to 3.26 mm were achieved. Al6061-T6 substrate with a thickness of 12.6 mm was used.

Copper samples were produced in N₂ by varying the gas pressure and temperature (Table 3). Using the conditions given in Table 3, Cu powder was deposited on a 115 mm x 90 mm area x 9.5 mm thickness C110000 Cu alloy substrate (commercially pure copper) using a serpentine raster pattern with a 1 mm line separation. After machining the top surfaces of the samples, deposition thicknesses were 7.0 mm, 9.0 mm, and 9.1 mm, for Cu-1, Cu-2, and Cu-3, respectively.

Furthermore, an Oseir HiWatch HR1 (Tampere, Finland) particle shadow image velocimetry system was used for measuring the size dependent particle velocity under all

Table 1 VRC nozzles organized with respect to recommended powder feedstock and gas type combinations along with measured expansion region dimensions

Nozzles	Feedstock	Gas	Throat Diameter (mm)	Expansion Section Length (mm)	Physical Area Expansion Ratio
NZZL0070	Al6061	N ₂	2.00	150	10.3
NZZL0071	Al6061	He	1.75	150	8.2
NZZL0058	Cu	N ₂	1.75	142	8.7

Table 2 CS process conditions for the deposition of Al6061 blocks with model estimated average particle impact velocity (V_p) and ratio of impact velocity to critical velocity (V_p/V_{cr})

Sample No	Nozzle	Gas	P (bar)	T (°C)	Substrate Prep	V_p (m/s)	V_p/V_{cr}
Al-1-1	NZZL0070	N ₂	68	445	Machine Finish, IPA Wash	821	1.1
Al-1-2	NZZL0070	N ₂	68	445	Sand Blast, IPA Wash	821	1.1
Al-1-3	NZZL0070	N ₂	68	445	Wire Wheel, IPA Wash	821	1.1
Al-1-4	NZZL0070	N ₂	68	445	Wire Wheel, IPA Wash, Preheat	821	1.1
Al-2-1	NZZL0071	He	35	445	Wire Wheel, IPA Wash	1260	1.4

Table 3 CS process conditions for the deposition of Cu blocks with model estimated average particle impact velocity (V_p) and ratio of impact velocity to critical velocity (V_p/V_{cr})

Sample No	Nozzle	Gas	P (bar)	T (°C)	Substrate Prep	V_p (m/s)	V_p/V_{cr}
Cu-1	NZZL0058	N ₂	50	368	Wire Wheel, IPA Wash, Preheat	638	1.4
Cu-2	NZZL0058	N ₂	60	484	Wire Wheel, IPA Wash, Preheat	694	1.6
Cu-3	NZZL0058	N ₂	65	600	Wire Wheel, IPA Wash, Preheat	735	1.8

combinations of CS process settings given in Tables 1 and 2 to validate induced variability in particle velocity. The measurements were conducted 25 mm downstream of the exit plane of the nozzle without the presence of a substrate prior to the manufacturing of CS processed samples in each condition.

Ultrasound Wave Velocity Measurements

Ultrasound measurements were conducted using a Baker Hughes-Waygate Technologies (Hürth, Germany) Mentor UT phased array measurement system. Ultrasound Testing (UT) was used for through thickness ultrasound wave velocity measurements. The wave velocity measurements are possible for coatings and deposits with known thicknesses. A feasibility assessment was first conducted to test whether a first reflection signal can be reliably detected from the coating/substrate interface by carefully adjusting ultrasound system parameters. This test was conducted as represented in the diagram given in Fig. 1.

The tests were conducted with a pulse/echo UT probe which was designed to emit ultrasound waves with a wave frequency of 5 MHz. Pulse/echo probes can generate ultrasound waves and receive these signals. The waveform expected to be observed by the UT probe receiver is given

in Fig. 1(b) for the testing mode shown in Fig. 1(a) if the deposition/substrate interface is detectable. Through an exhaustive feasibility study, it was possible to repeatably and reliably detect Reflection 2 and Reflection 3, as shown in Fig. 1(a), and measure the wave travel times t_1 , t_2 , and t_3 (Fig. 1b). This allows for wave velocity calculations for deposits with known thickness values. Wave velocity through the deposition can be calculated as:

$$c_{deposit} = \frac{2 \cdot d_{deposit}}{t_2 - t_1} \tag{Eq 1}$$

where $c_{deposit}$ is the through thickness ultrasonic longitudinal wave velocity of the deposit and $d_{deposit}$ is the known deposition thickness. Ultrasound wave velocity measurements were also conducted on Al6061-T6 and Cu substrates.

Ultrasound wave velocity measurements provide a through thickness measurement method for determining the bulk deposition quality for a known thickness material. However, the minimum thickness that can be reliably measured is dependent on the probe frequency and the wave velocity. In the case of the 5 MHz probe and the measured wave velocities of wrought Al6061 (6038 m/s) and Cu (4497 m/s), the minimum thickness that can be reliably measured is ~ 1.2 mm for Al6061 and ~ 0.9

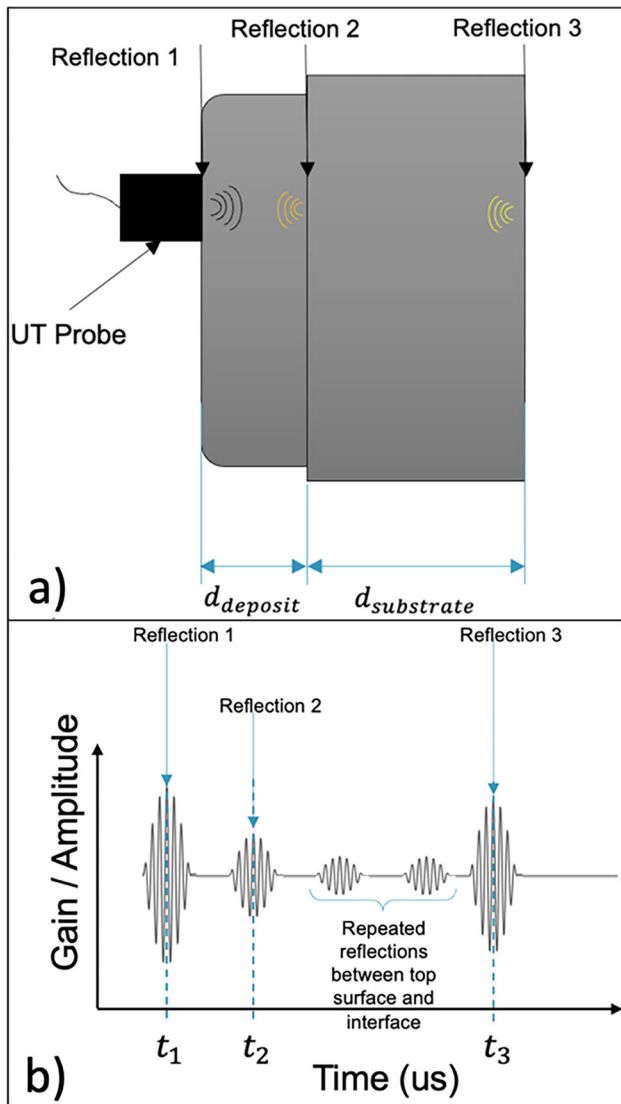


Fig. 1 (a) Diagram showing a pulse/echo UT probe that is sending an ultrasound wave signal through a deposition-substrate material system and features that would be expected to cause wave reflections. (b) The sketch of the expected ultrasound waveform received by the pulse/echo UT probe

mm for Cu. It is expected that, with some degree of porosity and unbonded region in particle-particle interfaces (Ref 36), CS deposited material will cause the wave propagation speed to reduce and allow for smaller thickness values to be measured. Nevertheless, in the presented work, minimum measured deposition thickness values were 5.09 mm for Al6061 and 4.35 mm for copper, which are well within the capabilities of the hardware. For both Al6061 and Cu blocks, ultrasound wave velocity measurements were collected regionally at four corners and the center with three measurements taken in each region with a total of 15 measurements. The longitudinal wave velocity measurements were then used for predicting the elastic

moduli of the deposits using Eq 2 to compare with elastic moduli measured with tensile tests.

$$E = \frac{\rho c_{\text{deposit}}^2 (1 + \nu)(1 - 2\nu)}{1 - \nu} \quad (\text{Eq 2})$$

In Eq 2, E is the elastic modulus, c_{deposit} is the longitudinal wave velocity within the deposit, and ν is the Poisson's ratio. Poisson's ratio for Al6061 and pure Cu were assumed to be the same as wrought materials as 0.350 and 0.355, respectively (Ref 42). The non-porous density of Al6061 and Cu was taken as 2.70 g/cm³ and 8.96 g/cm³, respectively (Ref 43). For the determination of elastic modulus using Eq 2, the density term (ρ) was adjusted using measured porosity (Section “Porosity Measurements”) and the reported material density (ρ_r) as $\rho = (1 - \text{porosity})\rho_r$.

Electrical Conductivity Measurements

Two eddy current systems were used to conduct electrical conductivity measurements on machined surfaces of CS deposited samples. The first of these systems was a Jentek (Marlborough, MA) 8000 eddy current array system. The Jentek system uses continuum electromagnetic models and meandering winding magnetometer (MWM) arrays based on these models (Ref 44, 45). When the MWM sensor contacts the sample surface, the interruption of the magnetic field appears on an impedance plane. The design of the eddy current coils (Fig. 2b) and the continuum models allow for the response to be correlated with sensor lift-off and electrical conductivity, which are handled by the equipment. This enables a reliable measurement of electrical conductivity with only air calibration.

The second means of electrical conductivity measurements were accomplished by an Olympus N600C (Shinjuku City, Tokyo, Japan) eddy current measurement system, which uses two reference materials for calibration purposes. In this work, 16.95 MS/m and 35.23 MS/m reference blocks were used to calibrate the eddy current electrical conductivity probe that's used at a frequency of 60 kHz.

Unlike in ultrasound measurements, eddy currents form near the surface as a function of the probe frequency and the electrical and magnetic properties of the material. Eddy current depth of penetration (δ) can be written as in Eq 3.

$$\delta = \frac{1}{\sqrt{\pi f \mu \sigma}} \quad (\text{Eq 3})$$

In Eq 3, depth of penetration is a function of probe frequency (f), magnetic permeability (μ), and electrical conductivity (σ). In the case of nonmagnetic materials, such as Al6061 and Cu, magnetic permeability is 1.257 ·

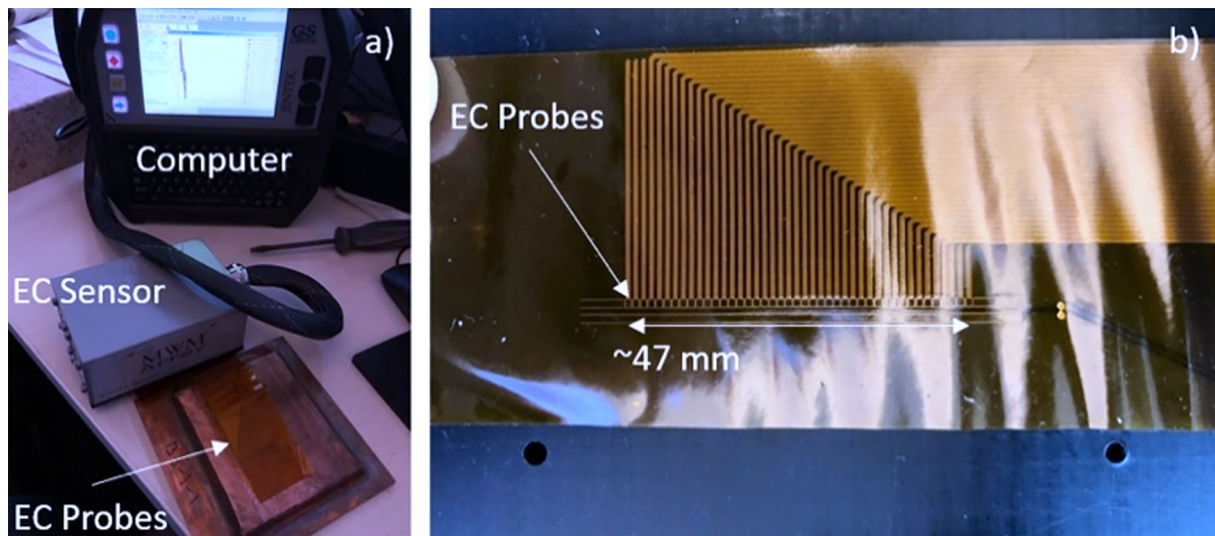


Fig. 2 (a) Jentek MWM Eddy Current NDT/NDE setup. (b) Image showing the EC Probes

10^{-6} H/m, which is equivalent to magnetic permeability in free space (Ref 46). In MWM measurements, the AC frequency was set to 251.1 kHz for Al6061 samples, which is equivalent to a depth of penetration of ~ 0.25 mm for lower conductivity nitrogen sprayed samples and ~ 0.20 mm for higher conductivity helium sprayed samples. While the MWM system can operate at lower frequencies, for copper specimens, 199.5 kHz AC frequency was used which has an equivalent depth of penetration of ~ 0.18 mm. Using the conventional Olympus system with 60 kHz AC frequency yields a measurement depth range of 0.53 mm to 0.39 mm for low conductivity samples (15 MS/m) to high conductivity samples (27.2 MS/m). While eddy current electrical conductivity measurements are quick, easy to use, and reliable, the method is limited to near surface measurements.

On each Al6061 and Cu sample, 470 measurements were taken with the Jentek MWM EC array sensors (47 probes) at 10 different locations on the surfaces of the samples. The linear array was arranged along the width of the sample and relocated 10 mm away after each measurement along the length of the sample. The results were spatially analyzed, and no significant differences were found. Therefore, the data were pooled per sample. In the case of the Olympus N600C single probe measurements, twelve measurements evenly distributed on the machine finished surfaces of the samples were taken. Like the MWM measurements, the data were pooled per sample.

Porosity Measurements

Specimens were extracted from aluminum and copper deposits perpendicular to the direction of the deposit. The metallographic sample preparation was conducted in

accordance with ASTM E3 (Ref 47). The porosity of the coating was measured using a Zeiss AxioScope 7 digital optical microscope (Oberkochen, Germany). Porosity measurements were conducted automatically using a color contrast threshold method and by computing the porous region area percentage using the Zeiss ZenCore image processing software.

Hardness Measurements

Hardness measurements were conducted on polished cross sections of samples in the in-plane direction (perpendicular to the spray direction). The measurements were conducted at 200-gram load using a Pace Technologies (Tucson, AZ) Alpha-MHT-1000Z micro-Vickers hardness testing instrument.

Tensile Strength Measurements

Aluminum and copper samples were tested using a Shimadzu (Kyoto, Japan) universal floor standing tensile test machine with a 100 kN load cell. Strain data were collected using an Epsilon 3542-0100-050-ST contact extensometer made by Epsilon Technology Corp. (Jackson, WY). Flat subsize tensile specimens were manufactured per ASTM E8/E8M-16a (Ref 48). Before testing, both the extensometer and the load cell were calibrated using the Shimadzu TRAPEZIUM-X software connected to the testing machine. The samples were pulled at a loading rate of 0.5 mm/min until failure.

Fractography

Following tensile testing, fractography using scanning electron microscopy (SEM) was conducted to examine the topography of fractured surface of dog bone tensile specimens. Sonic cleaning was done before viewing fractured dog bone tensile specimens under SEM to remove any debris or contaminants from the surfaces of the samples. After sonic cleaning, sample surfaces were investigated at fracture sites using a Thermo Scientific™ Scios Dual-Beam SEM (Waltham, MA, USA) with a magnification range of 800X to 5000X, using an accelerating voltage of 5 kV and a beam current of 0.10 nA.

Results and Discussion

Velocity Measurements

Particle velocity measurements show that the helium spray of aluminum (Al-2-1) produces a much higher average particle velocity in comparison with the nitrogen spray cases (Al-1-X). With the increased particle velocity, the deposition quality is also expected to increase in terms of porosity, tensile strength, and ductility (Ref 13).

In the three copper spray cases, gas pressure and temperature were incrementally increased to achieve incremental increase in particle impact velocity as given in Table 3. Figure 4 shows that the average measured particle velocity incrementally increased as 640 m/s, 675 m/s, and 706 m/s for Cu-1, Cu-2, and Cu-3, respectively.

Overall, the plots in Fig. 3 and 4 highlight the controlled change in velocity with the adjustment of gas dynamic parameters as given in the experimental design (Tables 2 and 3).

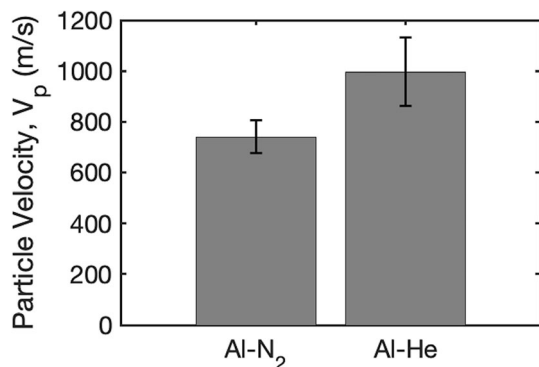


Fig. 3 Mean and standard deviation of Al6061 particle velocity for nitrogen (Al-1-X) and helium (Al-2-1) spray cases

Ultrasound Wave Velocity Measurements

The results obtained from measuring ultrasound measurements (Fig. 5) show that through thickness longitudinal wave velocity ($c_{deposit}$) is primarily influenced by the impact velocity increase associated with the use of He. Al-2-1 generates $c_{deposit}$ that is roughly equal to that of the wrought commercially pure aluminum (Ref 49) and is much higher than those of Al-1-X series samples (Fig. 5) indicating an improvement (i.e., reduction) in porosity, particle–particle interfacial quality, and/or an increase in the elastic properties of the material. Furthermore, in the case of Al-2-1, the acoustic wave signal reflecting from deposit/substrate interface was weak and therefore the signal amplitude needed to be increased significantly (25 dB to 40 dB) in comparison with the Al-1-X series samples to extract $c_{deposit}$. This suggests that the interfacial quality in the case of Al-2-1 is better in comparison with Al-1-X series samples. Statistical analysis of variance indicates that the Al-1-X samples do not produce means

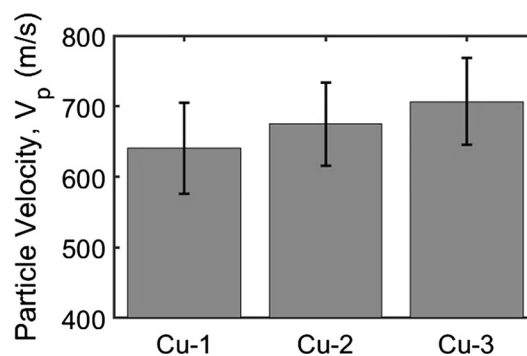


Fig. 4 Mean and standard deviation of copper particle velocity for Cu-1, Cu-2, and Cu-3, respectively

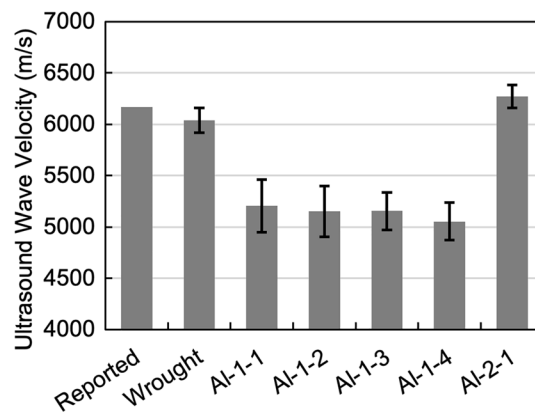


Fig. 5 Longitudinal wave velocity measurement of aluminum samples are plotted with one standard deviation error bars. CS sample results are compared with measurements from a wrought Al6061 specimen and the reported longitudinal wave velocity for commercially pure Al [49]

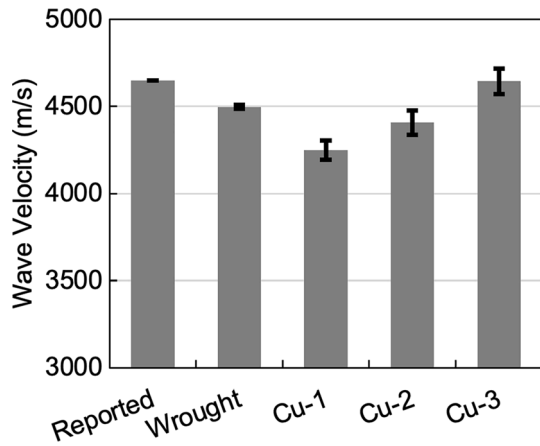


Fig. 6 Longitudinal wave velocity measurements of Cu-1, Cu-2, and Cu-3 samples are plotted with one standard deviation error bars. CS sample results are compared with measurements from a wrought copper specimen and reported copper longitudinal wave velocity [49]

that are significantly different, which indicates that the substrate surface preparation method did not induce a significant change in ultrasound wave velocity. Therefore, the change in the amplitude of the signal response from the deposit/substrate interface is primarily associated with an increase in the particle impact velocity in Al-2-1.

The $c_{deposit}$ readings for copper samples (Fig. 6) clearly correlate with particle impact velocity. $c_{deposit}$ is found to increase correspondingly with increase in carrier gas pressure, temperature, and particle impact velocity. Similar to the Al6061 samples, it is expected that this increase in $c_{deposit}$ is indicative of improvements in porosity, particle–particle interfacial quality, and/or an increase in the elastic properties of the material Eq 2, which are further discussed with the results of destructive tests.

Electrical Conductivity Measurements

Electrical conductivity measurement results from the Jentek and Olympus systems are given in Fig. 7. The results are plotted along with the electrical conductivity of wrought Al6061 as reported (Ref 46) and measured with the Jentek system.

High electrical conductivity reading in Al-2-1 cold spray sample indicates that the deposit is dense and has few defects like porosity, micro cracks near the surface. Electrical conductivity measurements conducted on Al6061 specimens validate the finding that electrical conductivity correlates to changes in the particle impact velocity. The lack of variation among the Al-1-X samples is expected, as process conditions were identical, except for surface preparation.

Figure 8 clearly shows that there is a positive correlation between the particle impact velocity and the electrical

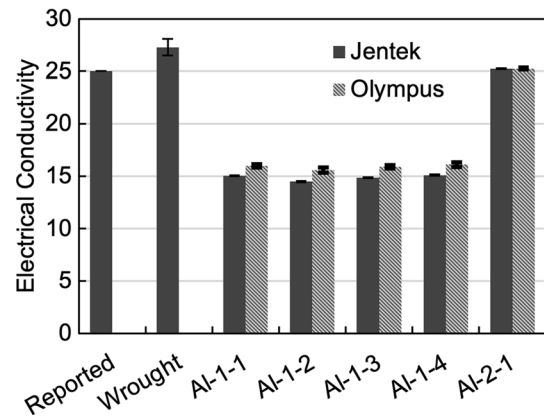


Fig. 7 Electrical conductivity of aluminum specimens of wrought, Al6061-T6, Al-1-1, Al-1-2, Al-1-3, Al-1-4, Al-2-1 as measured with Jentek and Olympus systems. The values are plotted along with the reported electrical conductivity of Al6061-T6 [46]

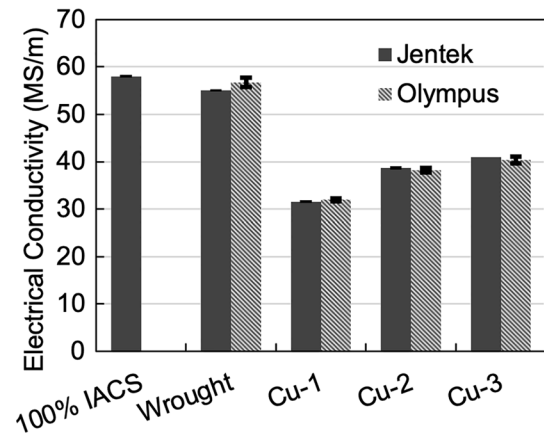


Fig. 8 Electrical conductivity of copper specimens Cu-1, Cu-2, Cu-3 as measured with Jentek and Olympus systems. 100% IACS is the international annealed copper standard reported as 58.2 MS/m [50]

conductivity readings from Cu samples. As the particle impact velocity increases, the porosity of the deposit decreases, and the density increases, resulting in a higher electrical conductivity.

In Al6061 and Cu cases, Jentek and Olympus systems provide very similar results and both systems appear to provide good sensitivity to the changes in the particle impact velocity. This shows that cross platform eddy current measurement of electrical conductivity is reliable.

Porosity Measurements

In Fig. 9, porosity levels among Al6061 samples are compared. Among nitrogen sprayed samples, subtle differences can be seen with the average porosity values between 1.1 to 1.5%. However, an analysis of variance showed the differences in the means are not statistically

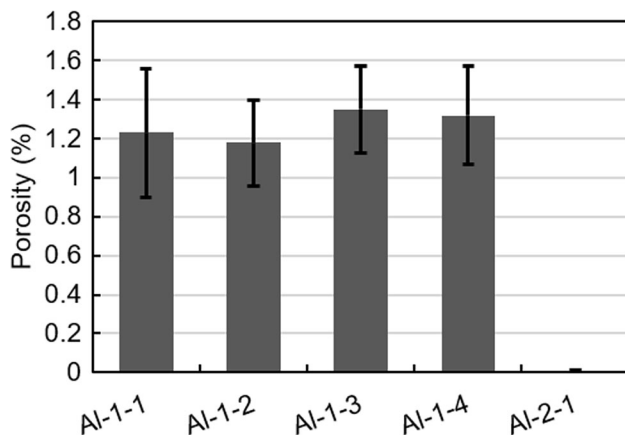


Fig. 9 Porosity measurement results for Al6061 samples

significant based on the variance. The helium sprayed Al-2-1, however, presented practically no porosity.

Porosity levels and the microstructure of Al6061 samples can be seen in sample microscope images after polishing and etching in Fig. 10. Particle–particle interfaces and pores are clear in nitrogen sprayed Al6061 samples (Fig. 10a–d) while the helium sprayed sample microscope image (Fig. 10e) shows good particle–particle interfaces that are not as clearly defined due to improved material adhesion. Additionally, practically no porosity is visible in the helium deposited Al-2-1 sample.

Figure 11 shows that the porosity in the copper samples dropped incrementally and they have a negative correlation with the increase in particle impact velocity. While the sample produced with the lowest impact velocity (Cu-1) showed the highest level of porosity at 1.04%, the sample that was deposited with the highest particle impact velocity (Cu-3) showed the lowest porosity at 0.34%. Cross sectional microscope images from etched samples can be seen in Figure 12 for copper samples. While the interface quality looks similar in all samples, the sizes of pores appear to decrease from Cu-1 sample to Cu-3 sample (Fig. 12a–c) which follows the trend of the porosity measurement results given in Fig. 11.

Reduction in porosity in Al6061 and Cu associated with the increase in impact velocity also directly correlates with increase in ultrasound wave velocity and electrical conductivity. Reduction in porosity of as deposited CS samples associated with process parameters (e.g., increasing impact velocity) also indicate improvements in particle–particle bonding strength (Ref 51).

Hardness Measurements

Figure 13(a) shows that Al-2-1, which was produced using helium and high particle impact velocities, has a higher hardness value than its nitrogen sprayed counterparts (Al-

1-x series), which were produced with lower particle impact velocities (Fig. 3). Figure 13(a) additionally shows that the mean hardness values of the Al-1-x sample series are close to each other. The difference among the samples was tested using an analysis of variance, which showed that there was no statistical significance to the differences with a 95% confidence interval. Similarly, for the copper specimens, incremental increase in particle impact velocity affects the hardness value of the resulting deposit. Higher impact velocities are expected to induce more strain hardening. This is apparent in the incremental increase in hardness from Cu-1 to Cu-3 samples (Fig. 13b).

Tensile Strength Measurements

Ultimate tensile strength and modulus of elasticity of aluminum samples are plotted in Fig. 14, which shows that the Al-2-1 sample prepared using He as the carrier gas has significantly higher ultimate tensile strength due to increased particle impact velocity when compared to the Al-1-X series samples (Fig. 3). The differences among the tensile strength of the nitrogen sprayed Al-1-X series samples are not statistically significant. Al-1-X samples showed ~ 0.14% while Al-2-1 samples showed ~ 5.16% elongation indicating increased ductility for samples sprayed with He. Average modulus of elasticity of samples ranged between 55 GPa and 66 GPa with an overall average of 59 GPa. Although the helium sprayed sample (Al-2-1) appears to have a slightly higher modulus of elasticity, a statistical analysis of variance with a 95% confidence level indicates that the average modulus between all N₂ and He samples are not significantly different.

Noting that the modulus of elasticity is statistically the same and the porosity difference between the nitrogen sprayed Al-1-X specimens and the helium sprayed Al-2-1 specimens are approximately 1.3%, the roughly 15% increase in ultrasound wave velocity is suggested to be largely due to improved particle–particle adhesion and a reduction in unbonded interfacial regions, which also results in a significant increase in the ultimate tensile strength. The improvement in the microstructure due to increased impact velocity in the He spray case is clear in Fig. 10 with increased particle deformation, interparticle contact area, and reduced porosity. To directly consider any possible effects of modulus in wave speed, the difference in the moduli of Al-1-1 (lowest modulus) and Al-2-1 (highest modulus) is allowed to be significant. When considered so, the change in the elastic modulus between the two cases (Fig. 14b) accounts for approximately 8% of the 15% increase in the ultrasound wave velocity according to the relationship calculated by Eq 2 (Fig. 5). This indicates that the slight increase in the elastic modulus cannot

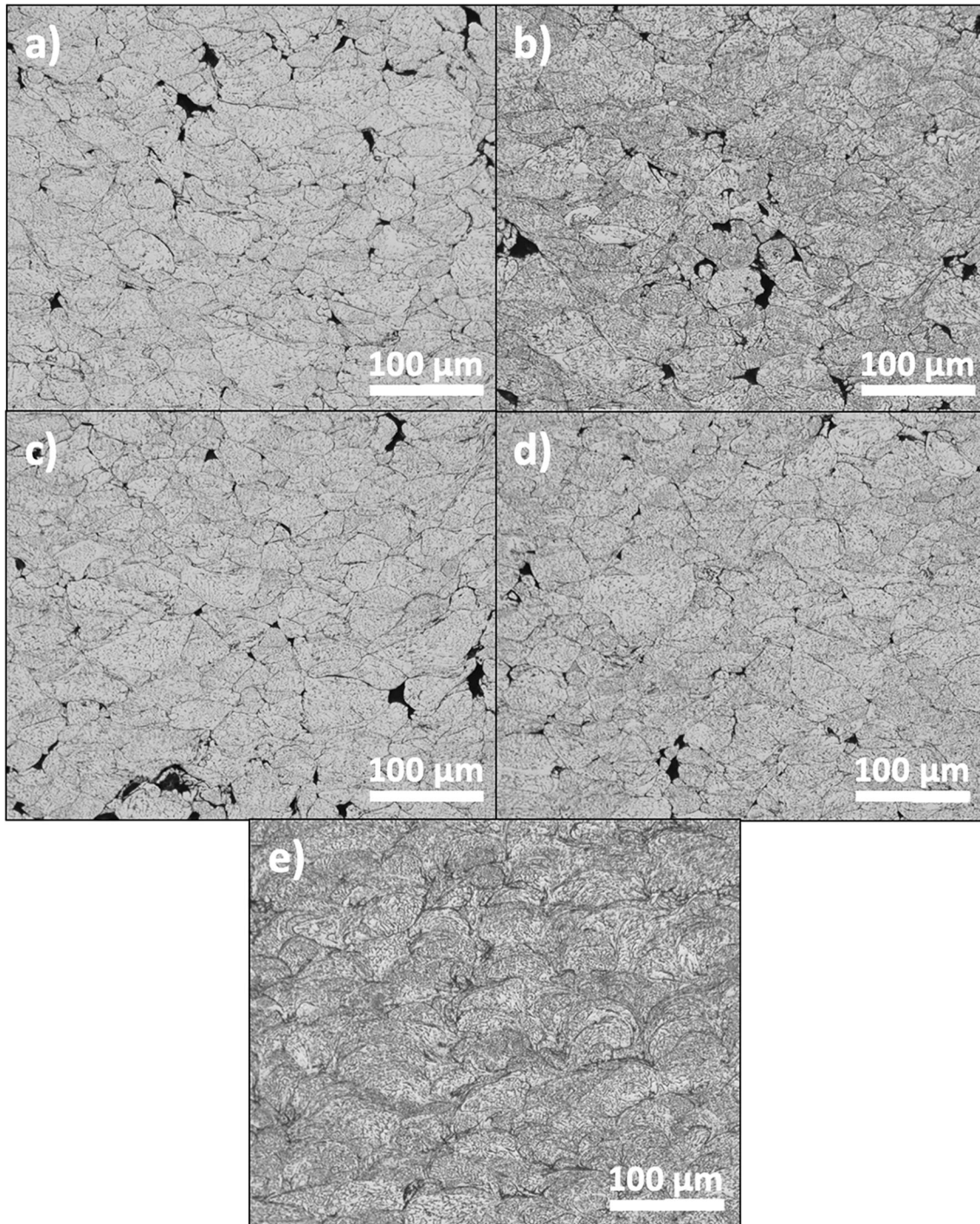


Fig. 10 Sample cross sectional microscope images from (a) Al-1-1, (b) Al-1-2, (c) Al-1-3, (d) Al-1-4, and (e) Al-2-1 samples after polishing and etching

account for all the increase in ultrasound wave velocity and that unbonded regions at particle–particle interfaces and the increase in porosity cause reduction in wave velocity. Furthermore, this observation indicates that the changes associated with particle–particle bonding quality can be

captured via ultrasound wave velocity measurements non-destructively and quantitatively.

Furthermore, the estimation of elastic modulus by ultrasound wave velocity using Eq 2 (Fig. 14b) suggests that the elastic modulus should be lower than measured for N_2

sprayed samples (Al-1-X) and significantly higher for He sprayed samples (Al-2-1). However, the elastic modulus is statistically the same for all Al6061 samples. Therefore, the discrepancy between the measured elastic modulus and the modulus estimated by using Eq 2 in N₂ sprayed samples can be attributed to the poor particle–particle bonding and porosity. In helium sprayed specimens, there is practically no

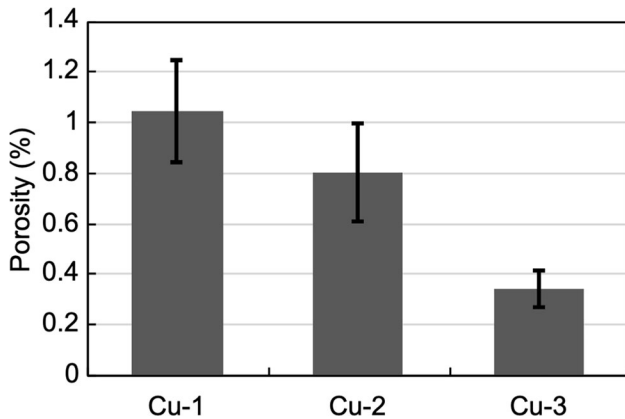


Fig. 11 Porosity measurement results for copper samples

difference between the measured elastic modulus and that predicted by Eq 2. The near wrought ultimate tensile strength, elastic modulus, and the reduction in porosity indicate that the use of He, which enables high impact velocities, yields significant improvements in interfacial bonding. Moreover, the ultrasound wave velocity measurements were only conducted in the through thickness direction (Fig. 1) while the uniaxial tensile tests represent properties in the in-plane direction. A certain degree of anisotropy is expected between the in-plane (parallel to the substrate surface) versus the out-of-plane (orthogonal to the substrate surface) directions (Ref 52), which may also account for some of the discrepancy between the $c_{deposit}$ indicated and measured elastic modulus in nitrogen sprayed specimens. However, this effect appears to dissipate with increased particle impact velocity in He sprayed specimens (Fig. 15) further indicating that the increase in ultrasound wave velocity is largely associated with improved particle–particle adhesion and reduced porosity.

In Cu specimens, gas pressure and temperature are increased to increase particle impact velocity (Fig. 4). A higher impact velocity results in improved bonding, leading to an increase in ultimate tensile strength (Fig. 15a).

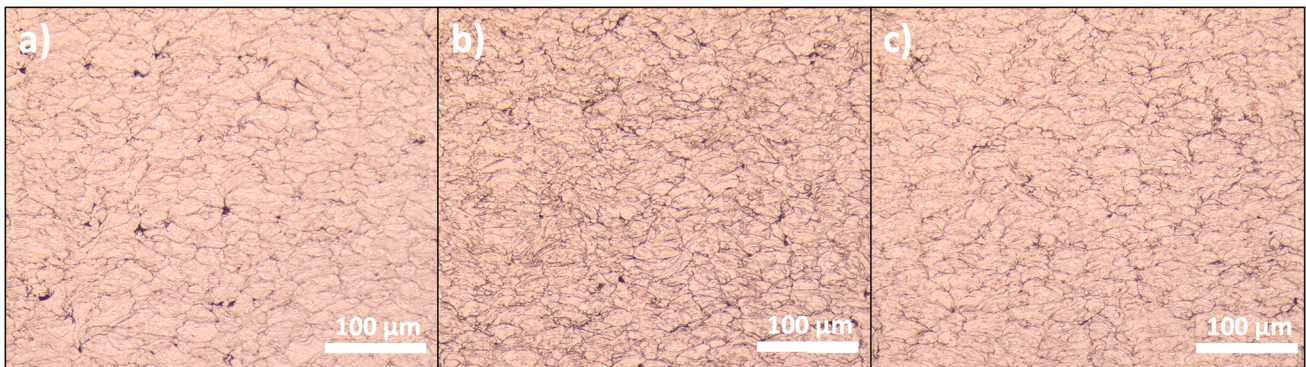


Fig. 12 Sample cross sectional microscope images from (a) Cu-1, (b) Cu-2, and (c) Cu-3 samples after polishing and etching

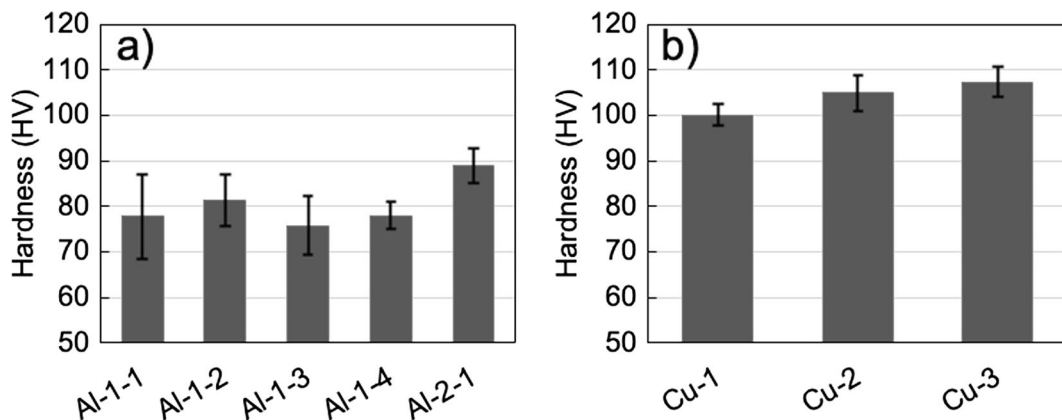


Fig. 13 Mean and one standard deviation from hardness measurements of (a) Al6061 and (b) Cu samples

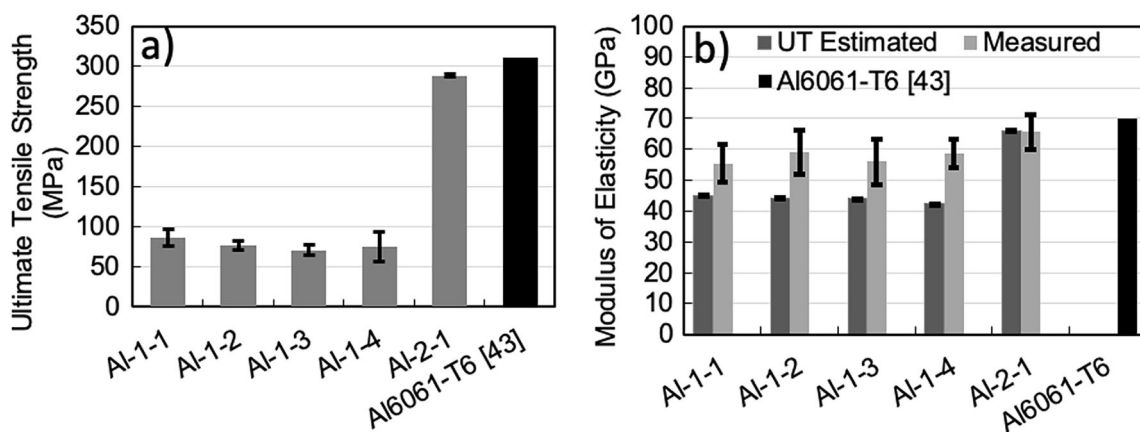


Fig. 14 (a) Ultimate tensile strength and (b) modulus of elasticity of aluminum alloy 6061 samples given with error bars indicating one standard deviation. Modulus of elasticity estimated by ultrasound wave velocity measurements (Figure 5) and using (2) are also plotted

in (b) with error bars indicating variability introduced by the variability in the wave velocity measurements given by one standard deviation. In (a) and (b) wrought Al6061-T6 tensile strength and elastic modulus are plotted for comparison

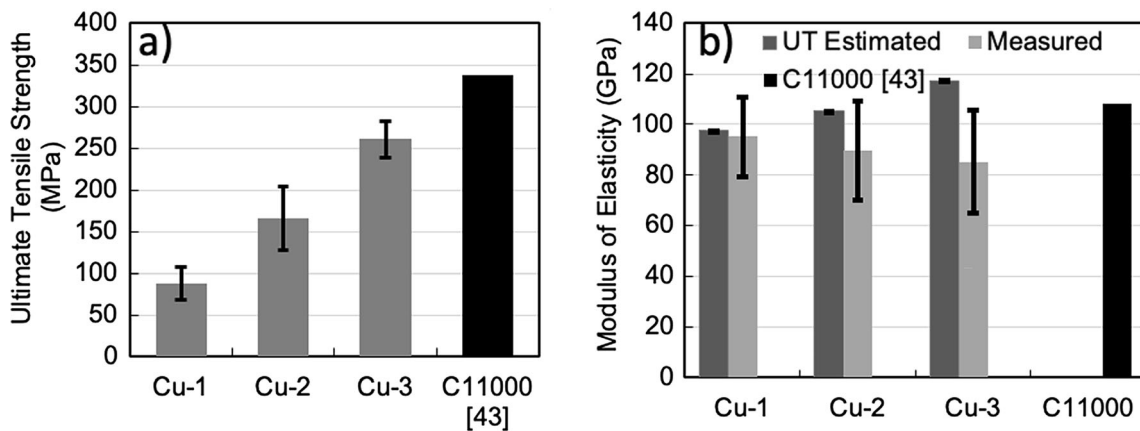


Fig. 15 (a) Ultimate tensile strength and (b) modulus of elasticity measurements of copper specimens given with error bars indicating one standard deviation. Modulus of elasticity estimated by ultrasound wave velocity measurements (Figure 6) and using Eq 2 are also

plotted in (b) with error bars indicating variability introduced by the variability in the wave velocity measurements given by one standard deviation. In (a) and (b) wrought C11000 tensile strength and elastic modulus are plotted for comparison

This effect is exemplified by the low strength of Cu-1 (low impact velocity) and the high strength of Cu-3 (high impact velocity). Cu-1, Cu-2, and Cu-3 samples showed 0.09, 0.21, and 0.41% ductility indicating mostly brittle fracture with minor incremental increase in ductility. From Cu-1 to Cu-3, average modulus of elasticity dropped approximately 10 GPa. However, due to the large variability among samples, this difference does not appear to be statistically significant according to an analysis of variance with a confidence level of 95%.

As in Al6061 elastic modulus analysis, the ultrasound wave velocity increase should point to an improvement in the elastic modulus. However, measurements show that the elasticity of the material stays statistically constant between samples that were produced with incrementally increasing particle impact velocity. In CS, the feedstock particles retain much of their internal microstructure when

consolidated except in the particle–particle interfacial regions where severe plastic deformation is experienced (Ref 53) unless in extreme cases where ratio of impact velocity to critical velocity is far above unity ($V_p/V_{cr} \gg 1$), which is not the case in our experiments where $V_p/V_{cr} < 1.5$ (Ref 40). This can reasonably explain why the measured elastic modulus stays approximately the same while the ultrasound wave velocity increases in both Al6061 and Cu samples. Therefore, the increase in ultrasound wave velocity can largely be attributed to improved adhesion between particles and reduced porosity.

Fractography

Al-1-x series samples that are manufactured using the nitrogen carrier gas have smooth, featureless appearances, and although deformed, the curved surfaces of gas

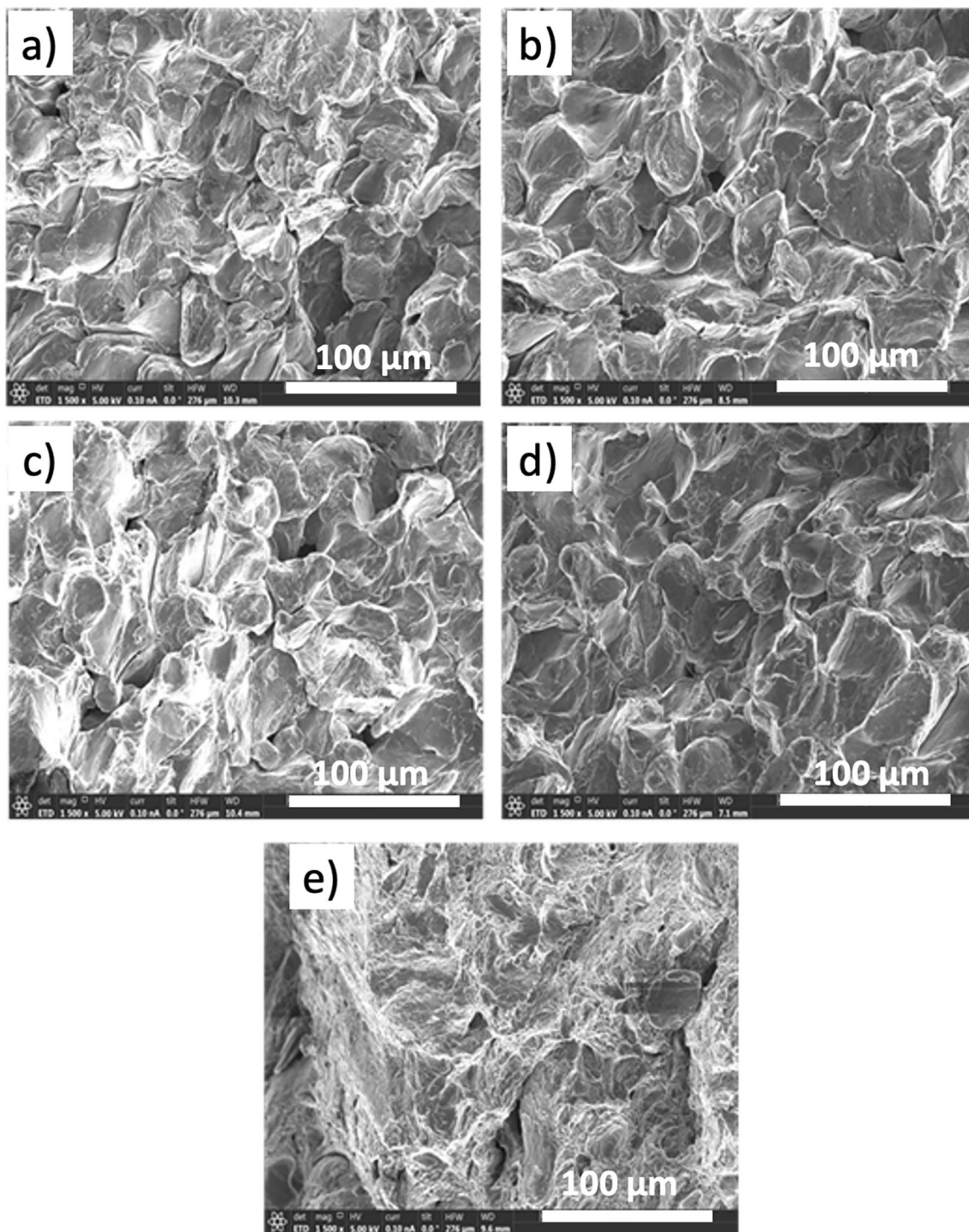


Fig. 16 SEM images taken at 1500x magnification from the fractured surfaces of tensile specimens of (a) Al-1-1, (b) Al-1-2, (c) Al-1-3, (d) Al-1-4, and (e) Al-2-1

atomized spherical particles are visible (Fig. 16a-d). This shows that fracture occurs mainly at particle–particle interfaces in a brittle manner. As seen in Fig. 16(e), SEM image of Al-2-1 sample that was manufactured using helium carrier gas has a rough, dimpled appearance and is showing signs of ductile fracture. The fractography

analysis further confirms the brittle failure experienced in N_2 sprayed samples and the lower interface quality captured in tensile tests. Fractography analysis also confirms that adhesion between particles is greatly improved in He sprayed Al-2-1 specimens, which further solidifies our argument in ultrasound wave velocity and eddy current

electrical conductivity measurements capturing the improvement in particle–particle adhesion.

The fractured surface of copper specimens is studied under SEM with a magnification of 1500x. As seen from Fig. 17, fractured surfaces were typically smooth, and the deformed particles and particle pull outs are also distinguishable. This indicates brittle fracture at particle–particle boundaries. In fractography analysis of Cu specimens, the improvement in the particle–particle behavior is not as clearly defined as Al6061 samples. However, the improvement in ultimate tensile strength given by Fig. 15(a) is a clear indication that the results in Cu specimens are in line with those with Al6061 specimens with improvement in particle–particle adhesion, which is detected with both ultrasound wave velocity and electrical conductivity measurements.

Conclusions

In this work, nondestructive ultrasound longitudinal wave velocity and eddy current electrical conductivity measurement methods have been studied for their sensitivity in detecting changes associated with destructively measured metrics of porosity, hardness, and tensile strength in cold spray (CS) produced specimens. The conclusions from this work can be summarized as follows.

- Both ultrasound wave velocity and eddy current readings exhibit incremental increase associated with incremental increase in particle impact velocity, which was manipulated with the control of gas dynamic parameters using a fluid dynamic model and validated through particle image velocimetry.
- Increases in through-thickness ultrasound wave velocity and electrical conductivity correlate with reduction in porosity and increase in hardness, which were improved because of increased particle impact velocity.

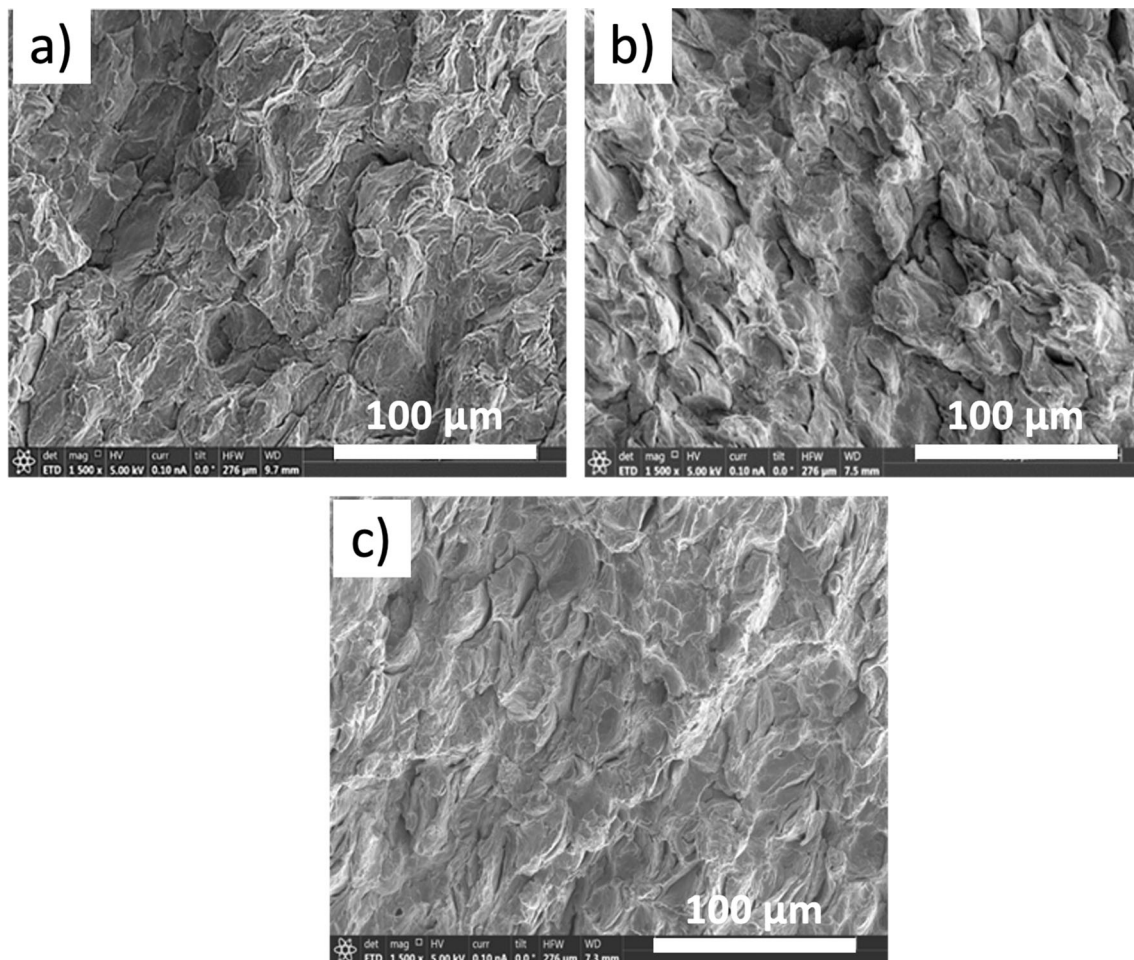


Fig. 17 SEM images taken at 1500x magnification from the fractured surfaces of tensile specimens of (a) Cu-1, (b) Cu-2, and (c) Cu-3

- This connection is further supported by correlating ultimate tensile strength measurements with quantitative nondestructive measurements. Increase in particle impact velocity leads to an increase in ultimate tensile strength in both Al6061 and Cu specimens, which are directly correlated with increases in ultrasound wave velocity and eddy current electrical conductivity measurements. Scanning electron microscope images from fracture surfaces of Al6061 samples reveal that a substantial increase in the ratio of impact velocity to critical velocity in He-sprayed specimens results in predominantly ductile fracture, whereas N₂-sprayed samples exhibit brittle fracture. This aligns with an enhancement in elongation to fracture (>5%) in He-sprayed specimens. However, the elastic modulus between N₂ and He sprayed samples stay statistically the same, which indicates that the majority of the ductility comes from improvement in reduction in porosity and improvement in particle–particle adhesion, which is clearly picked up by ultrasound wave velocity measurements. The improvement in tensile characteristics of the CS deposited specimens is also correlated with electrical conductivity.
- In Cu specimens, elongation remains generally low (<0.5%), with a marginal incremental increase corresponding to higher particle impact velocity. Due to the overall brittle fracture and a slight change in ductility associated with increased impact velocity, detecting improvements in particle–particle adhesion qualitatively in SEM analysis of fracture surfaces poses challenges. Nonetheless, the clear incremental increases in ultimate tensile strength and the relatively constant elastic modulus indicate improvements in porosity and particle–particle adhesion strength, which are identified through ultrasound wave velocity and eddy current electrical conductivity measurements.
- This study suggests that ultrasound measurement of longitudinal acoustic wave velocity is yielding itself as a powerful tool for quantitatively detecting the through thickness quality of CS deposited parts across regions of known thickness. However, it is important to note that ultrasound testing is useful beyond a minimum thickness defined by the acoustic frequency of the ultrasound probe and the wave velocity across the material of interest. Modeling the wave propagation may also be necessary for complicated geometries.
- Furthermore, the ultrasound method, through this work, has been proven to be effective in nondestructively and quantitatively detecting the through thickness quality of thick coatings, structures, and repairs while completely intact with the substrate even in similar deposition/substrate material combinations.
- Electrical conductivity measurement via eddy current systems, on the other hand, also prove to be a useful tool in predicting the quality of deposits near the test surface.
- Finally, it is expected that this work, among others, will aid in developing the generalized standards and quality control measures necessary for increased confidence in CS and other additive manufacturing processes.

Acknowledgments This research was funded by the Army Research Laboratory under the Cooperative Agreement Number W911NF-20-2-0024-CLIN003. The views and conclusions contained in this document are those of the authors and should not be interpreted as representing the official policies, either expressed or implied, of the Army Research Laboratory or the U.S. Government. The U.S. Government is authorized to reproduce and distribute reprints for Government purposes notwithstanding any copyright notation herein.

Funding Open access funding provided by Northeastern University Library.

Open Access This article is licensed under a Creative Commons Attribution 4.0 International License, which permits use, sharing, adaptation, distribution and reproduction in any medium or format, as long as you give appropriate credit to the original author(s) and the source, provide a link to the Creative Commons licence, and indicate if changes were made. The images or other third party material in this article are included in the article's Creative Commons licence, unless indicated otherwise in a credit line to the material. If material is not included in the article's Creative Commons licence and your intended use is not permitted by statutory regulation or exceeds the permitted use, you will need to obtain permission directly from the copyright holder. To view a copy of this licence, visit <http://creativecommons.org/licenses/by/4.0/>.

References

1. K. Ito and Y. Ichikawa, Microstructure Control of Cold-Sprayed Pure Iron Coatings Formed Using Mechanically Milled Powder, *Surf. Coat. Technol.*, 2019, **357**, p 129-139. <https://doi.org/10.1016/j.surfcoat.2018.10.016>
2. A. Sova, R. Maestracci, M. Jeandin, P. Bertrand, and I. Smurov, Kinetics of Composite Formation Process in Cold Spray: Modelling and Experimental Validation, *Surf. Coat. Technol.*, 2017, **318**, p 309-314.
3. C.A. Widener et al., Application of High-Pressure Cold Spray for an Internal Bore Repair of a Navy Valve Actuator, *J. Therm. Spray Technol.*, 2016, **25**(1-2), p 193-201.
4. Z. Khalkhali and J.P. Rothstein, Characterization of the Cold Spray Deposition of a Wide Variety of Polymeric Powders, *Surf. Coat. Technol.*, 2020, **383**, p 125251. <https://doi.org/10.1016/j.surfcoat.2019.125251>
5. D. Chatelain, A. Denoirjean, V. Guipont, F. Rossignol, and N. Tessier-Doyen, *Role of PEEK as Intermediate Layer in the Cold*

- Spray of Hydroxyapatite Coating*, *J. Spray Technol, Therm*, 2023. <https://doi.org/10.1007/s11666-023-01622-1>
6. R.C. Dykhuizen and M.F. Smith, Gas Dynamic Principles of Cold Spray, *J. Therm. Spray Technol.*, 1998, **7**(2), p 205-212.
 7. K. Sakaki and Y. Shimizu, Effect of the Increase in the Entrance Convergent Section Length of the Gun Nozzle on the High-Velocity Oxygen Fuel and Cold Spray Process, *J. Therm. Spray Technol.*, 2000, **10**(3), p 487-496.
 8. A.P. Alkhimov, V.F. Kosarev, and S.V. Klinkov, The Features of Cold Spray Nozzle Design, *J. Therm. Spray Technol.*, 2001, **10**(2), p 375-381.
 9. H. Assadi, F. Gärtner, T. Klassen, and H. Kreye, Comment on 'Adiabatic Shear Instability is not Necessary for Adhesion in Cold Spray', *Scripta Mater.*, 2019, **162**, p 512-514. <https://doi.org/10.1016/j.scriptamat.2018.10.036>
 10. H. Assadi, F. Gartner, T. Stoltenhoff, and H. Kreye, Bonding Mechanism in Cold Gas Spraying, *Acta Mater.*, 2003, **51**, p 4379-4394.
 11. Q. Chen et al., High-Strain-Rate Material Behavior and Adiabatic Material Instability in Impact of Micron Scale Al-6061 Particles, *J. Therm. Spray Technol.*, 2018, **27**, p 641-653.
 12. S. Yin, P. Cavaliere, B. Aldwell, R. Jenkins, H. Liao, and W. Li, Cold Spray Additive Manufacturing and Repair: Fundamentals and Applications, *Addit. Manuf.*, 2018, **21**, p 628-650.
 13. V. Champagne, O. Ozdemir, and A. Nardi, Eds. *Practical Cold Spray*. Springer International Publishing, 2021.
 14. S. Camilleri et al. (2023) What is 'good' metal AM? Exploring the industry's value metrics for production. *Metal Additive Manufacturing*. 137-149. Available: <https://www.metal-am.com/metal-additive-manufacturing-magazine-archive/metal-additive-manufacturing-vol-9-no-1-spring-2023/>
 15. A. Duguid, (2019) Materials and Properties for Additive Cold Spray. In: *Cold Spray Action Team Meeting*, US Army Research Laboratory, Worcester, MA, USA
 16. C.A. Widener, O.C. Ozdemir, and M. Carter, Structural Repair Using Cold Spray Technology for Enhanced Sustainability of High Value Assets, *Proc. Manuf.*, 2018, **21**, p 361-368.
 17. O. A. Britton, (2013) Repair of External Aircraft Panels and Surface Characterization of Cold Spray Depositions for Cold Spray/Epoxy Adhesion, M.S., South Dakota School of Mines and Technology, Rapid City
 18. M. Yandouzi, S. Gaydos, D. Guo, R. Ghelichi, and B. Jodoin, Aircraft Skin Restoration and Evaluation, *J. Therm. Spray Technol.*, 2014, **23**(8), p 1281-1290. <https://doi.org/10.1007/s11666-014-0130-1>
 19. R. Sinclair-Adamson, V. Luzin, A. Duguid, K. Kannorpatti, and R. Murray, Residual Stress Distributions in Cold-Spray 3D-Printed Parts, *J. Therm. Spray Technol.*, 2020, **29**, p 1525-1537.
 20. S.C. Altuparmak and B. Xiao, A Market Assessment of Additive Manufacturing Potential for the Aerospace Industry, *J. Manuf. Process.*, 2021, **68**, p 728-738. <https://doi.org/10.1016/j.jmapro.2021.05.072>
 21. B.C. Sousa, M.A. Gleason, B. Haddad, V.K. Champagne, A.T. Nardi, and D.L. Cote, Nanomechanical Characterization for Cold Spray: From Feedstock to Consolidated Material Properties, *Metals*, 2020, **10**(9), p 1195.
 22. I. Gibson, (2021) Additive manufacturing technologies, D. W. Rosen, B. Stucker, and M. Khorasani, Eds., Third edition / Ian Gibson, David Rosen, Brent Stucker, Mahyar Khorasani. ed: Cham, Switzerland : Springer,
 23. C.V. Cojocararu et al., Dimensional Analysis and Laser-Ultrasonic Inspection of Cold Spray Additive Manufacturing Components, *Cold Spray in the Realm of Additive Manufacturing*. S. Pathak, G.C. Saha Ed., Springer International Publishing, Cham, 2020, p 219-243
 24. S.W. Glass et al., Cold Spray NDE for Porosity and Other Process Anomalies, *Pacific Northwest Nat. Lab.*, 2018, **10**(1063/1), p 5031507.
 25. H. Koivuluoto, A. Coleman, K. Murray, M. Kearns, and P. Vuoristo, High Pressure Cold Sprayed (HPCS) and Low Pressure Cold Sprayed (LPCS) Coatings Prepared from OFHC Cu Feedstock: Overview from Powder Characteristics to Coating Properties, *J. Therm. Spray Technol.*, 2012, **21**(5), p 1065-1075. <https://doi.org/10.1007/s11666-012-9790-x>
 26. G. Sundararajan, N.M. Chavan, G. Sivakumar, and P. Sudharshan Phani, Evaluation of Parameters for Assessment of Inter-Splat Bond Strength in Cold-Sprayed Coatings, *J. Therm. Spray Technol.*, 2010, **19**(6), p 1255-1266. <https://doi.org/10.1007/s11666-010-9527-7>
 27. S. Bagherifard et al., Tailoring Cold Spray Additive Manufacturing of Steel 316 L for Static and Cyclic Load-Bearing Applications, *Mater. Design*, 2021, **203**, p 109575. <https://doi.org/10.1016/j.matdes.2021.109575>
 28. K.-R. Donner, F. Gaertner, and T. Klassen, Metallization of Thin Al₂O₃ Layers in Power Electronics Using Cold Gas Spraying, *J. Therm. Spray Technol.*, 2011, **20**(1), p 299-306. <https://doi.org/10.1007/s11666-010-9573-1>
 29. T. Stoltenhoff, C. Borchers, F. Gärtner, and H. Kreye, Microstructures and Key Properties of Cold-Sprayed and Thermally Sprayed Copper Coatings, *Surf. Coat. Technol.*, 2006, **200**(16-17), p 4947-4960. <https://doi.org/10.1016/j.surfcoat.2005.05.011>
 30. T. Stoltenhoff, H. Kreye, and H.J. Richter, An Analysis of the Cold Spray Process and Its Coatings, *J. Therm. Spray Technol.*, 2001, **11**(4), p 542-550.
 31. J. Villafuerte Ed., *Modern Cold Spray: Materials, Process, and Applications*, Springer International Publishing AG, Cham, 2015
 32. M.R. Rokni, S.R. Nutt, C.A. Widener, V.K. Champagne, and R.H. Hrabe, Review of Relationship Between Particle Deformation, Coating Microstructure, and Properties in High-Pressure Cold Spray, *J. Therm. Spray Technol.*, 2017, **26**, p 1308-1355.
 33. Y.-J. Li, X.-T. Luo, H. Rashid, and C.-J. Li, A New Approach to Prepare Fully Dense Cu with High Conductivities and Anti-Corrosion Performance by Cold Spray, *J. Alloys Compd.*, 2018, **740**, p 406-413. <https://doi.org/10.1016/j.jallcom.2017.11.053>
 34. R.G. Maev, S. Titov, V. Leshchynsky, D. Dzhurinskiy, and M. Lubrick, In Situ Monitoring of Particle Consolidation During Low Pressure Cold Spray by Ultrasonic Techniques, *J. Therm. Spray Technol.*, 2011, **20**, p 845-851. <https://doi.org/10.1007/s11666-011-9631-3>
 35. P. L. Clavette, M. A. Klecka, A. T. Nardi, G. C. Ojard, and R. S. Gostautas, "Real Time NDE of Cold Spray Processing Using Acoustic Emission, In: *Structural Health Monitoring and Damage Detection, Volume 7*, Cham, C. Niezrecki, Ed., 2015// 2015: Springer International Publishing, pp. 27-36.
 36. F. Honarvar and A. Varvani-Farahani, A Review of Ultrasonic Testing Applications in Additive Manufacturing: Defect Evaluation, Material Characterization, and Process Control, *Ultrasonics*, 2020, **108**, p 106227. <https://doi.org/10.1016/j.ultras.2020.106227>
 37. H. Assadi et al., On Parameter Selection in Cold Spraying, *J. Therm. Spray Technol.*, 2011, **20**(6), p 1161-1176.
 38. O.Ç. Özdemir, J.M. Conahan, and S. Müftü, Particle Velocimetry, CFD, and the Role of Particle Sphericity in Cold Spray, *Coatings*, 2020, **10**(12), p 1254.
 39. T. Schmidt et al., From Particle Acceleration to Impact and Bonding in Cold Spraying, *J. Therm. Spray Technol.*, 2009, **18**(5-6), p 794-808.
 40. H. Assadi, H. Kreye, F. Gartner, and T. Klassen, Cold Spraying- A Materials Perspective, *Acta Mater.*, 2016, **116**(1), p 382-407.

41. O.C. Ozdemir, C.A. Widener, D. Helfritsch, and F. Delfanian, Estimating the Effect of Helium and Nitrogen Mixing on Deposition Efficiency in Cold Spray, *J. Therm. Spray Technol.*, 2016, **25**(4), p 660-671.
42. E. Oberg, F. D. Jones, H. L. Horton, H. H. Ryffel, C. J. McCauley, and L. Brengelman. () Machinery's Handbook (31st Edition), ed: Industrial Press.
43. J. R. Davis, Ed. (1997) *Concise Metals Engineering Data Book*. Materials Park, OH: ASM International
44. Goldfine, N. J., and Clark, D. (1996, November). Introduction to the Meandering Winding Magnetometer (MWM) and the grid measurement approach. In *Nondestructive Evaluation of Materials and Composites* (Vol. 2944, pp. 186-192). SPIE, <https://doi.org/10.1117/12.259057>.
45. N. J. Goldfine, J. T. Lovett, Y. Sheiretov, and P. J. Zombo, (1995) Dielectrometers and magnetometers suitable for in-situ inspection of ceramic and metallic coated components. In: *SPIE: Nondestructive Evaluation of Aging Maritime Applications*, Oakland, CA, USA,
46. J. R. Davis, () Table 4. Electrical Conductivity and Resistivity of Metals and Alloys," in *Metals Handbook, Desk Edition (2nd Edition)*: ASM International.
47. Standard Guide for Preparation of Metallographic Specimens, *ASTM, West Conshohocken, PA, USA, 2017*.
48. *Standard Test Methods for Tension Testing of Metallic Materials*, ASTM, West Conshohocken, PA, 2016.
49. M. J. Crocker, "47.4.3 Normal Modes," in *Handbook of Acoustics*: John Wiley & Sons.
50. C. Moosbrugger and F. Cverna, "Table 2.1 Volume Conductivity at Ambient Temperature of High Conductivity Material Families. In *ASM Ready Reference - Electrical and Magnetic Properties of Metals*: ASM International.
51. S. Rech, A. Trentin, S. Vezzu, E. Vedelago, J.G. Legoux, and E. Irissou, Different Cold Spray Deposition Strategies: Single-and Multi-Layers to Repair Aluminium Alloy Components, *J. Therm. Spray Technol.*, 2014, **23**, p 1237-1250. <https://doi.org/10.1007/s11666-014-0141-y>
52. N. Hutasoit, M.A. Javed, R.A.R. Rashid, S. Wade, and S. Palanisamy, Effects of Build Orientation and Heat Treatment on Microstructure, Mechanical and Corrosion Properties of Al6061 Aluminium Parts Built by Cold Spray Additive Manufacturing Process, *Int. J. Mech. Sci.*, 2021, **204**, p 106526. <https://doi.org/10.1016/j.ijmecsci.2021.106526>
53. M.R. Rokni, C.A. Widener, O.C. Ozdemir, and G.A. Crawford, Microstructure and Mechanical Properties of Cold Sprayed 6061 Al in As-Sprayed and Heat Treated Condition, *Surf. Coat. Technol.*, 2017, **309**, p 641-650.

Publisher's Note Springer Nature remains neutral with regard to jurisdictional claims in published maps and institutional affiliations.